# Effects of Turbulence and Devolatilization Models on Gasification Simulation

Armin Silaen
Research Assistant
asilaen@uno.edu

Ting Wang *
Professor
twang@uno.edu

Energy Conversion & Conservation Center
University of New Orleans
New Orleans, Louisiana, USA

## ABSTRACT

Numerical simulations of the oxygen-blown coal gasification process inside a generic entrained-flow gasifier are carried out using the commercial CFD solver FLUENT. The Navier-Stokes equations and seven species transport equations are solved with three heterogeneous global reactions and two homogeneous reactions. Finite rates are used for the heterogeneous solid-to-gas reactions. Both finite rate and eddy-breakup combustion models are calculated for each homogeneous gas-to-gas reaction, and the smaller of the two rates is used. Four different devolatilization models are employed and compared. The Kobayashi model produces slower devolatilization rate than the other models. The constant rate model produces the fastest devolatilization rate. The single rate model and the chemical percolation model produce moderate and consistent devolatilization rate. Slower devolatilization rate produces higher exit gas temperature, $H_2$, and $CO_2$, but lower CO and heating value, and hence, lower gasification efficiency. Combustion of volatiles is modeled with two-stage global reactions with an intermediate stage via benzene.

Turbulence models significantly affect the simulated results. Among five turbulence models tested, the standard k-ε and the RSM models give consistent results. The time scale for employing stochastic time tracking of particles also affects simulated result. Caution has to be exerted to select the appropriate time constant value. Smaller particles have a higher surface/volume ratio and react faster than larger particles. However, large particles possessing higher inertia could impinge on the opposing jet and change the thermal-flow filed and the reaction rates.

## 1.0 INTRODUCTION

Gasification is the process of converting various carbon-based feedstocks to clean synthetic gas (syngas), which is primarily a mixture of hydrogen ($H_2$) and carbon-monoxide (CO) as fuels, through an incomplete combustion. Feedstock is partially combusted with oxygen and steam at high temperature and pressure with only less than 30% of the required oxygen for complete combustion being provided. The syngas produced can be used as a fuel, usually as a fuel for boilers or gas turbines to generate electricity, or can be used to make a synthetic natural gas, hydrogen gas or other chemical products. The gasification technology is applicable to any type of carbon-based feedstock, such as coal, heavy refinery residues, petroleum coke, biomass, and municipal wastes.

The gas produced from coal gasification can be used for syngas or as a source for methanol and hydrogen, which are used in the manufacturing process of ammonia or hydrogenation applications in refineries. Another usage of syngas, which is gradually gaining more popularity, is using syngas as fuel in electricity generation by employing the Integrated Gasification Combined Cycle (IGCC). The syngas produced in the gasifier is cleaned and used as a fuel for gas turbines. The gas is burned with compressed air in the combustor of the gas turbine. The high pressure and hot gases produced in the combustor then expand through the gas turbine to drive the air compressor and an electric generator. The hot exhaust gases from the gas turbine are sent to a heat recovery steam generator (HRSG) to produce steam that expands through a steam turbine to drive another electric generator.

IGCC plants can achieve efficiencies of about 55% and low emissions, compared to 43-45% efficiencies and relatively higher emissions for regular or critical pulverized coal combustion power plants. Gasification integrated in IGCC is considered a clean and efficient alternative to coal combustion for power generation. The high-pressure and high-temperature syngas from the gasifier can especially take advantage of the new generation of advanced turbine systems (ATS), which require high compression ratio and high turbine inlet temperature to produce up to 60% combined cycle efficiency. Furthermore, the syngas can also be tapped to produce methanol and hydrogen.

### 1.1 Global Gasification Process

The main global reactions in a gasification process are given below (Smoot and Smith [1985]):

Heterogeneous (solid and gas) phase:

$C(s) + ½\ O_2 \rightarrow CO$, $\Delta H°_R = -110.5$ MJ/kmol (R1.1)

$C(s) + CO_2 \rightarrow 2CO$, $\Delta H°_R = +172.0$ MJ/kmol (Gasification, Boudouard reaction) (R1.2)

$C(s) + H_2O_{(g)} \rightarrow CO + H_2$, $\Delta H°_R = +131.4$ MJ/kmol (Gasification) (R1.3)

$C + 2H_2 \rightarrow CH_4$, $\Delta H°_R = -87.4$ MJ/kmol (Direct methanation) (R1.4)

Homogenous gas phase:

$CO + ½\ O_2 \rightarrow CO_2$, $\Delta H°_R = -283.1$ MJ/kmol (R1.5)

$CO + H_2O_{(g)} \rightarrow CO_2 + H_2$, $\Delta H°_R = -41.0$ MJ/kmol (Water-shift) (R1.6)

$CH_{1.952}O_{0.9278} \rightarrow 0.9278CO + 0.9399H_2 + 0.01203C_6H_6$ (Decomposition of volatiles) (R1.7)

$C_6H_6 + 3O_2 \rightarrow 6CO + 3H_2$ (R1.8)

In this study, the methanation reactions are not considered.

### 1.2 Recent Research

Chen et al. [2000] developed a comprehensive three-dimensional simulation model for entrained coal gasifiers which applied an extended coal gas mixture fraction model with the Multi Solids Progress Variables (MSPV) method to simulate the gasification reaction and reactant mixing process. The model employed four mixture fractions separately track the variable coal off-gas from the coal devolatilization, char-$O_2$, char-$CO_2$, and char-$H_2O$ reactions. Chen et al. performed a series of numerical simulations for a 200 ton per day (tpd) two-stage air blown entrained flow gasifier developed for an IGCC process under various operation conditions (heterogeneous reaction rate, coal type, particle size, and air/coal partitioning to the two stages).

Chen et al.'s model predicted that coal devolatilization and char oxidation were responsible for most of the carbon conversion (up to 80%) in the two-stage air blown entrained flow gasifier. It was found that carbon conversion was independent of devolatilization rate, sensitive to the chemical kinetics of heterogeneous reactions on the char surface, and less sensitive to a change in coal particle size. They found that increasing air ratio (or reducing equivalence ratio) leads to increased $CO_2$ and decreased CO and $H_2$ concentrations.

Chen et. al. [2000] also predicted that increasing the average coal particle size decreases the carbon conversion, which results in an increase in the exit gas temperature and lower heating value. They also predicted that dry feed yields more CO mole fraction than wet feed does due to injecting less moisture into the system. Chen et. al. model shows that an increase in the system pressure increases the average residence time due to the reduced average gas velocity that further results in increased particle residence time and increased carbon conversion.

Bockelie et al. [2002(a)] of Reaction Engineering International (REI) developed a CFD modeling capability for entrained flow gasifiers that focus on two gasifier configurations: single-stage down fired system and two-stage with multiple feed inlets. The model was constructed using GLACIER, an REI in-house comprehensive coal combustion and gasification tool. The basic combustion flow field was established by employing full equilibrium chemistry. Gas properties were determined through local mixing calculations and are assumed to fluctuate randomly according to a statistical probability density function (PDF) which is characteristic of turbulence. Gas-phase reactions were assumed to be limited by mixing rates for major species as opposed to chemical kinetic rates. Gaseous reactions were calculated assuming local instantaneous equilibrium. The particle reaction processes include coal devolatilization, char oxidation, particle energy, particle liquid vaporization and gas-particle interchange. The model also includes a flowing slag sub-model.

Silaen and Wang [2005] conducted numerical simulations of the coal gasification process inside a generic two-stage entrained-flow gasifier using the commercial CFD solver FLUENT. The 3-D Navier-Stokes equations and seven species transport equations are solved with eddy-dissipation combustion model. They investigated the effects of several parameters on gasification performance including coal mixture (slurry or dry powder), oxidant (oxygen-blown or air-blown), wall cooling, and various coal distributions between the two stages. The simulation results provide the temperature and species distributions inside the gasifier. The results indicate that coal-slurry feed is preferred over coal-powder feed to produce hydrogen. On the other hand, coal-powder feed is preferred over coal-slurry feed to produce carbon monoxide. The air-blown operation yields poor fuel conversion efficiency and the lowest syngas heating value due to air dilution. The effect of wall cooling has been shown insignificant on the exit gas composition and heating value. The fuel conversion efficiency of the case with coal distribution with 75% (first stage) vs. 25% (second stage) is better than the case with 50% vs. 50% coal distribution. They stated that a two-stage design has an advantage of the flexibility to adjust parameters to achieve desired performance.

In the continuation of that study, Silaen and Wang [2006] carried out a study that focuses on the effect of flow injection directions on the gasification performance using the same generic two-stage entrained flow gasifier. Horizontal injection direction was compared to downward and upward direction. The results reveal that the horizontal injection direction gives the best gasifier performance. Changing the direction of the first-stage injectors downward results in a carbon fuel conversion reduction, but produces more $H_2$. Changing the direction of the second-stage injectors, however, does little affect the overall flow patterns due to the smaller-quantity of coal injection (25%) and hence the gasifier performance is essentially insignificantly affected.

This study is the continuous work of Silaen and Wang [2005, 2006] and focuses on the effects of different parameters on gasification performance including turbulence models, devolatilization models, finite reaction rates, and solid coal sizes.

### 1.2 Present Study and Objectives

In the previous studies by Silaen and Wang [2005, 2006], the instantaneous gasification model of solid coal particles was used, which would result in solid-gas reaction faster than the actual process. In this study, the particle combustion model using the finite rate is incorporated. Since the char particle surface reaction is involved. The transports of CO concentration and heat from the surface layer to the surrounding gases will depend on the thermal-flow behavior. Therefore, turbulence modeling and stochastic tracking of fluctuating particles will affect the simulated results. In addition, the different coal particle size will affect coal surface/volume ratio and

result in different gasification performance. To shed some light on the effect of above variables, the objective of this study is to investigate the effects of different turbulence models, devolatilization models, coal particle diameters, reaction heat, and stochastic tracking time constant on the outcome of the simulation.

## 2.0 COMPUTATIONAL MODEL

### 2.1 Physical Characteristics of the Model and Assumptions

This research studies an entrained flow coal gasifier. The geometry and computational meshes of the simplified 2-D gasifier is shown in Fig. 1. Two opposing injectors are located near the bottom of the gasifier. The geometry of the 3-D gasifier is shown in Fig. 2(a). A comprehensive fundamental investigation starts on 2-D geometry. Based on the 2-D results, more adequate models are selected and implemented in the 3-D study. In the simulations, the buoyancy force is considered, varying fluid properties are calculated for each species and the gas mixture, and the walls are assumed impermeable and adiabatic. The flow is steady and no-slip condition (zero velocity) is imposed on wall surfaces.

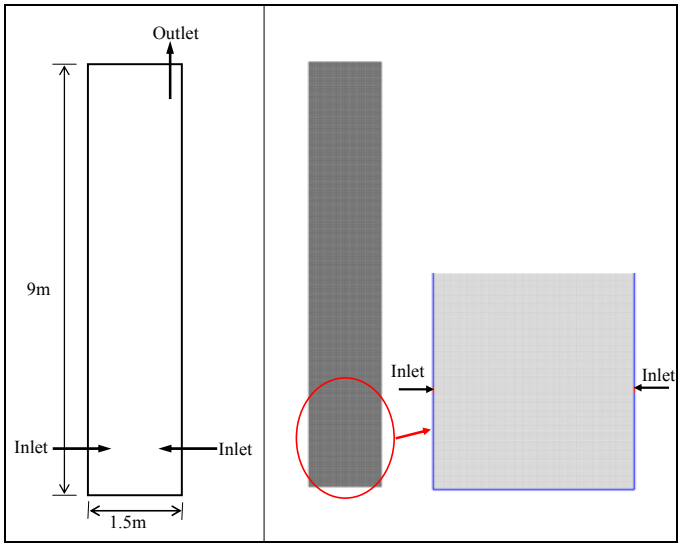


Fig. 1 Schematic of a simplified 2-D entrained flow gasifier and its meshed computational domain.

### Computational Setup

The meshed 2-D and 3-D computational domains are given in Figs. 1 and 2(b), respectively. A grid sensitivity study of both the 2-D and 3-D geometries is conducted. Four different 2-D grids including the coarse grid (33k cells), medium grid (86k cells), and fine grids (135k and 215k cells) are used. In the 3-D geometry, three different grids are used including the coarse grid (148k cells), medium grid (969k cells) and fine grid (1,684k cells).

The difference of temperature distributions for all four different grids in the 2-D geometry is very small, as shown in Fig. 3. Thus, to save the computational time, the medium grid of 86k cells is chosen as the grid for further parametric studies. The near-wall y+ of the 2-D grid is 118. The results of the 3-D geometries show that the temperature distributions of the medium and fine grids are almost identical. Again, to save computational time, the medium grid of 969k cells is chosen. The near-wall y+ of the 3-D grid is 190.

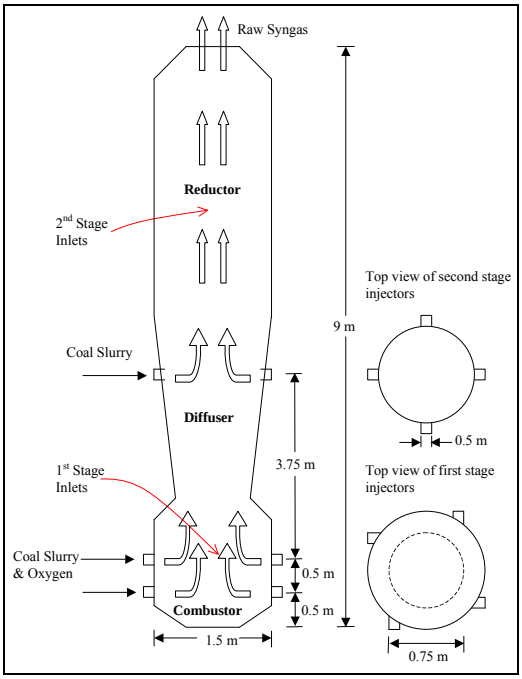


(a) Schematic of the 3-D gasifier

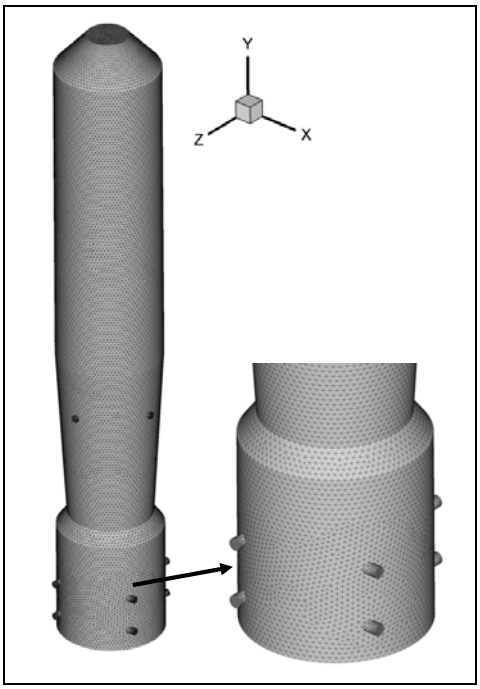


(b) Meshed 3-D computational domain

Fig. 2 (a) Schematics of 3-D one-stage entrained flow gasifier configuration studied, and (b) its meshed computational domain.

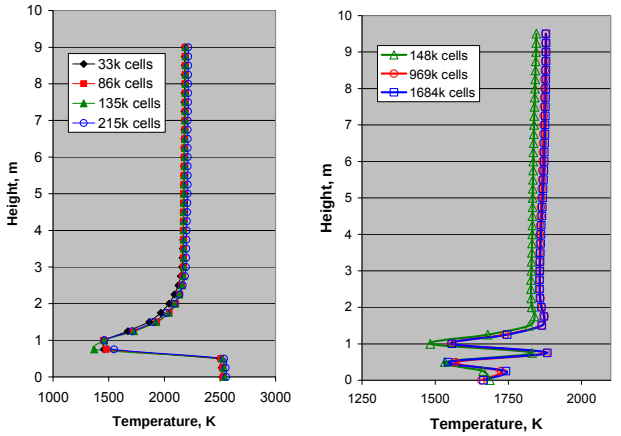


(a) 2-D (b) 3-D

Figure 3 Grid sensitivity study: temperature distributions for the different grid sizes of the 2-D and 3-D geometries.

## 2.2 Governing Equations

The time-averaged steady-state Navier-Stokes equations as well as the mass and energy conservation equations are solved. The governing equations for the conservations of mass, momentum and energy are given as:

$$\frac{\partial}{\partial x_i}\left(\rho u_{i\,j}\right) = S_m \tag{1}$$

$$\frac{\partial}{\partial x_i}\left(\rho u_i u_j\right) = \rho \bar{g}_j - \frac{\partial P}{\partial x_j} + \frac{\partial}{\partial x_i}\left(\tau_{ij} - \rho\overline{u_i' u_j'}\right) + F_j \tag{2}$$

$$\frac{\partial}{\partial x_i}\left(\rho c_p u_i T\right) = \frac{\partial}{\partial x_i}\left(\lambda \frac{\partial T}{\partial x_i} - \rho c_p \overline{u_i' T'}\right) + \mu\Phi + S_h \cdot \tag{3}$$

The symmetric stress tensor, $\tau_{ij}$, is given by

$$\tau_{ij} = \mu\left(\frac{\partial u_j}{\partial x_i} + \frac{\partial u_i}{\partial x_j} - \frac{2}{3}\delta_{ij}\frac{\partial u_k}{\partial x_k}\right) \cdot \tag{4}$$

The equation for species transport is

$$\frac{\partial}{\partial x_i}\left(\rho u_i C_j\right) = \frac{\partial}{\partial x_i}\left(\rho D_i \frac{\partial C_j}{\partial x_i} - \rho\overline{u_i' C_j'}\right) + S_j \cdot \tag{5}$$

## 2.3 Turbulence Models

Five turbulence models are considered including Standard k-ε, RNG (Re-Normalized Group) k-ε, Standard k-ω Model, Shear Stress Transport (SST) k-ω Model, and Reynolds Stress Model (RSM).

Standard k-ε Model -- The standard k-ε model defines the Reynolds stresses as

$$-\rho\overline{u_i' u_j'} = \mu_t\left(\frac{\partial u_i}{\partial x_j} + \frac{\partial u_j}{\partial x_i}\right) - \frac{2}{3}\rho k\delta_{ij} \tag{6}$$

where k is the turbulence kinetic energy, and $\mu_t$ is the turbulence viscosity given by

$$\mu_t = \rho C_\mu k^2 / \varepsilon \tag{7}$$

where $C_\mu$ is a constant and ε is the turbulence dissipation rate. The equations for the turbulence kinetic energy (k) and dissipation rate (ε) are

$$\frac{\partial}{\partial x_i}\left(\rho u_i k\right) = \frac{\partial}{\partial x_i}\left[\left(\mu + \frac{\mu_t}{\sigma_k}\right)\frac{\partial k}{\partial x_i}\right] + G_k - \rho\varepsilon \tag{8}$$

$$\frac{\partial}{\partial x_i}\left(\rho u_i \varepsilon\right) = \frac{\partial}{\partial x_i}\left[\left(\mu + \frac{\mu_t}{\sigma_\varepsilon}\right)\frac{\partial \varepsilon}{\partial x_i}\right] + C_{1\varepsilon}G_k\frac{\varepsilon}{k} - C_{2\varepsilon}G_k\rho\frac{\varepsilon^2}{k} . \tag{9}$$

$G_k$ is the generation of turbulence kinetic energy due to the mean velocity gradients.

The turbulent heat flux and mass flux can be modeled with the turbulent heat conductivity ($\lambda_t$) and the turbulent diffusion coefficient ($D_t$), respectively.

$$\rho c_p \overline{u_i' T'} = -\lambda_t \frac{\partial T}{\partial x_i} = -c_p \frac{\mu_t}{Pr_t}\frac{\partial T}{\partial x_i}, \tag{10}$$

$$\rho\overline{u_i' C'} = -\rho D_t \frac{\partial C}{\partial x_i} = -\frac{\mu_t}{Sc_t}\frac{\partial C}{\partial x_i} . \tag{11}$$

The constants $C_{1\varepsilon}$, $C_{2\varepsilon}$, $C_\mu$, $\sigma_k$, and $\sigma_\varepsilon$ used are: $C_{1\varepsilon}$ = 1.44, $C_{2\varepsilon}$ = 1.92, $C_\mu$ = 0.09, $\sigma_k$ = 1.0, $\sigma_\varepsilon$ =1.3 [[Launder and Spalding, 1972]. The turbulence Prandtl number, $Pr_t$, is set to 0.85, and the turbulence Schmidt number, $Sc_t$, is set to 0.7.

Enhanced Wall Function – The above k-ε model is mainly valid for high Reynolds number fully turbulent flow. Special treatment is needed in the region close to the wall. The enhanced wall function is one of several methods that model the near-wall flow. In the enhanced wall treatment, the two-layer model is combined with the wall functions. The whole domain is separated into a viscosity-affected region and a fully turbulent region by defining a turbulent Reynolds number, $Re_y$,

$$Re_y = yk^{1/2} / \nu \tag{12}$$

where k is the turbulence kinetic energy and y is the distance from the wall. The standard k-ε model is used in the fully turbulent region where $Re_y > 200$, and the one-equation model of Wolfstein [25] is used in the viscosity-affected region with $Re_y < 200$. The turbulent viscosities calculated from these two regions are blended with a blending function (θ) to smoothen the transition.

$$\mu_{t,enhanced} = \theta\mu_t + (1-\theta)\mu_{t,l} \tag{13}$$

where $\mu_t$ is the viscosity from the k-ε model of high Reynolds number, and $\mu_{t,l}$ is the viscosity from the near-wall one-equation model. The blending function is defined so it is equal to 0 at the wall and 1 in the fully turbulent region. The linear (laminar) and logarithmic (turbulent) laws of the wall are also blended to make the wall functions applicable throughout the entire near-wall region. A similar thermal wall function equation is employed for temperature calculation.

Reynolds Stress Model – Near the region of slurry coal injection, the interaction between the opposing or neighboring jets could be anisotropic and non-equilibrium with multiscaled integral and dissipation length scales.

Therefore, the Reynolds stress model (RSM), a second-moment closure, is considered in this study. The Reynolds stress transport equation can be given as

$$\frac{\partial}{\partial x_k}\left(\rho u_k \overline{u'_i u'_j}\right) = -\frac{\partial}{\partial x_k}\left[\rho u_k \overline{u'_i u'_j u'_k} + \overline{P(\delta_{kj}u'_i + \delta_{ik}u'_j)} + \mu\frac{\partial}{\partial x_k}\left(\overline{u'_i u'_j}\right)\right] - \rho\left(\overline{u'_i u'_k}\frac{\partial u_j}{\partial x_k} + \overline{u'_j u'_k}\frac{\partial u_i}{\partial x_k}\right) + \overline{P\left(\frac{\partial u'_i}{\partial x_j} + \frac{\partial u'_j}{\partial x_i}\right)} - 2\mu\overline{\frac{\partial u'_i}{\partial x_k}\frac{\partial u'_j}{\partial x_k}} \quad (14)$$

The diffusive term on the right-hand side can be modeled as

$$-\frac{\partial}{\partial x_k}\left[\rho u_k \overline{u'_i u'_j u'_k} + \overline{P(\delta_{kj}u'_i + \delta_{ik}u'_j)} + \mu\frac{\partial}{\partial x_k}\left(\overline{u'_i u'_j}\right)\right] = \frac{\partial}{\partial x_k}\left(\frac{\mu_t}{\sigma_k}\frac{\partial}{\partial x_k}\left(\overline{u'_i u'_j}\right)\right) \quad (15)$$

The second term on the right-hand side of Eq. (14) is the production term, and it is notated as $G_{ij}$

$$G_{ij} = -\rho\left(\overline{u'_i u'_k}\frac{\partial u_j}{\partial x_k} + \overline{u'_j u'_k}\frac{\partial u_i}{\partial x_k}\right) \quad (16)$$

The third term is the pressure-strain term, which can be modeled as

$$\overline{P\left(\frac{\partial u'_i}{\partial x_j} + \frac{\partial u'_j}{\partial x_i}\right)} = C_1\rho\frac{\varepsilon}{k}\left(\overline{u'_i u'_j} - \frac{2}{3}\delta_{ij}k\right) - C_2\left[A_{ij} - \frac{1}{3}\delta_{ij}A_{kk}\right] \quad (17)$$

where $A_{ij} = G_{ij} - \frac{\partial}{\partial x_k}\left(\rho u_k \overline{u'_i u'_j}\right)$. The constants $C_1$ and $C_2$ are 1.8 and 0.6, respectively. The last term in Eq. (14) can be approximated by

$$2\mu\overline{\frac{\partial u'_i}{\partial x_k}\frac{\partial u'_j}{\partial x_k}} = \frac{2}{3}\delta_{ij}\rho\varepsilon \quad (18)$$

and assumes this dissipation term isotropic.

Modeling of the turbulent heat flux and mass flux are similar as in the k-ε model. The turbulent kinetic energy and its dissipation rate can be calculated from the Reynolds stresses.

Other Models -- Ignoring details here, the turbulent models adopted in this study also include the RNG k-ε model, k-ω model, and the shear-stress transport (SST) k-ω model. RNG k-ε model was derived using renormalization group theory [Choudhury, 1993]. It has an additional term in the ε-equation to improve the accuracy for rapidly strained flows. It uses the effective viscosity to account for low-Reynolds-number effects. Theoretically, this model is more accurate and reliable than the standard k-ε model. The standard k-ω model is an empirical model based on transport equations for the turbulence kinetic energy (k) and the specific dissipation rate (ω), which can also be considered as the ratio of ε to k [Wilcox, D.C., 1998]. The low-Reynolds-number effect is accounted for in the k-ω model. The SST model is mixture of the k-ω model and the k-ε model: close to the wall it becomes the k-ω model while in the far field the k-ε model is applied [Menter, 1993].

### 2.4 Discrete Phases (Coal Particles or Liquid Droplets)

Discrete phases include coal particles and liquid droplets. Langrangian method to track each particle is adopted in this study.

Particles in the airflow can encounter inertia and hydrodynamic drags. Because of the forces experienced by a droplet in a flow field, the particles can be either accelerated or decelerated. The velocity change can be formulated by

$$m_p d\mathbf{v_p}/dt = \mathbf{F_d} + \mathbf{F_g} + \mathbf{F_o} \quad (19)$$

where $\mathbf{F_d}$ is the drag of the fluid on the droplet and $\mathbf{F_g}$ is the gravity. $\mathbf{F_o}$ represents the other body forces, typically include the "virtual mass" force, thermophoretic force, Brownian force, Saffman's lift force, etc.$\mathbf{V_p}$ is the particle velocity (vector).

(A) For coal particles

Gasification or combustion of coal particles undergoes the following global processes: (i) evaporation of moisture, (ii) devolatilization, (iii) gasification to CO and (iv) combustion of volatiles, CO, and char.

The rate of depletion of solid due to a surface reaction is expressed as,

$$\overline{R} = A\eta Y R \quad (20)$$

$$R = k\left(p_n - \frac{R}{D}\right)^N \quad (21)$$

where

$\overline{R}$ = rate of particle surface species depletion (kg/s)
A = particle surface area ($m^2$)
Y = mass fraction of surface the solid species in the particle
η = effectiveness factor (dimensionless)
R = rate of particle surface species reaction per unit area ($kg/m^2$-s)
$p_n$ = bulk partial pressure of the gas phase species (Pa)
D = diffusion rate coefficient for reaction
k = kinetic rate of reaction (units vary)
N = apparent order of reaction.

The kinetic rate of reaction is defined as

$$k = AT^n e^{-(E/RT)} . \quad (22)$$

The rate of particle surface species depletion for reaction order N = 1 is given by

$$\overline{R} = A\eta Y p_n \frac{kD}{D+k} . \quad (23)$$

For reaction order N = 0,

$$\overline{R} = A\eta Y k . \quad (24)$$

(B) For liquid droplets

When the coal slurry is injected through the injectors, the water is assumed to be atomized into small droplets. Theoretically, evaporation occurs at two stages: (a) when temperature is higher than the saturation temperature (based on local water vapor concentration), water evaporates from the droplet's surface, and the evaporation

is controlled by the water vapor partial pressure until 100% relative humidity is achieved; (b) when the boiling temperature (determined by the air-water mixture pressure) is reached, water continues to evaporate even though the relative humidity reaches 100%. After the moisture is evaporated due to either high temperature or low moisture partial pressure, the vapor diffuses into the main flow and is transported away. The rate of vaporization is governed by concentration difference between surface and gas stream, and the corresponding mass change rate of the droplet can be given by,

$$\frac{dm_d}{dt} = \pi d^2 k_c (C_s - C_\infty) \quad (25)$$

where $k_c$ is the mass transfer coefficient and $C_s$ is the concentration of the vapor at the particle's surface, which is evaluated by assuming that the flow over the surface is saturated. $C_\infty$ is the vapor concentration of the bulk flow, obtained by solving the transport equations. The values of $k_c$ can be calculated from empirical correlations by [Ranz and Marshall, 1955]:

$$Sh_d = \frac{k_c d}{D} = 2.0 + 0.6 Re_d^{0.5} Sc^{0.33}. \quad (26)$$

where Sh is the Sherwood number, Sc is the Schmidt number (defined as ν/D), D is the diffusion coefficient of vapor in the bulk flow. $Re_d$ is the Reynolds number, defined as uν/d, u is the slip velocity between the droplet and the gas.

When the droplet temperature reaches the boiling point, the following equation can be used to evaluate its evaporation rate [Kuo, 1985]:

$$\frac{dm_d}{dt} = \pi d^2 \left(\frac{\lambda}{d}\right)(2.0 + 0.46 Re_d^{0.5}) \ln\left(1 + c_p (T_\infty - T)/h_{fg}\right)/c_p \quad (27)$$

where λ is the heat conductivity of the gas/air, and $h_{fg}$ is the droplet latent heat. $c_p$ is the specific heat of the bulk flow.

The droplet temperature can also be changed due to heat transfer between droplets and the continuous phase. Without considering radiation heat transfer, the droplet's sensible heat change depends on the convective heat transfer and latent heat ($h_{fg}$), as shown in the following equation.

$$m_p c_p \frac{dT}{dt} = \pi d^2 h (T_\infty - T) + \frac{dm_p}{dt} h_{fg} \quad (28)$$

where the convective heat transfer coefficient (h) can be obtained with a similar empirical correlation to Eq. 29:

$$Nu_d = \frac{hd}{\lambda} = 2.0 + 0.6 Re_d^{0.5} Pr^{0.33} \quad (29)$$

where Nu is the Nusselt number, and Pr is the Prandtl number.

Stochastic Tracking of Particles -- The various turbulence models are based on the time-averaged equations. Using this flow velocity to trace the droplet will result in an averaged trajectory. In the real flow, the instantaneous velocity fluctuation would make the droplet dance around this average track. However, the instantaneous velocity is not calculated in the current approach as the time averaged Navier-Stokes equations are solved. One way to simulate the effect of instantaneous turbulence on droplets dispersion is to use the stochastic tracking scheme [Fluent, 2006]. Basically, the droplet trajectories are calculated by using the instantaneous flow velocity ($\bar{u} + u'$) rather than the average velocity ($\bar{u}$). The velocity fluctuation is then given as:

$$u' = \zeta\left(\overline{u'^2}\right)^{0.5} = \zeta(2k/3)^{0.5} \quad (30)$$

where ζ is a normally distributed random number. This velocity will apply during a characteristic lifetime of the eddy ($t_e$), given from the turbulence kinetic energy and dissipation rate. After this time period, the instantaneous velocity will be updated with a new ζ value until a full trajectory is obtained. When the stochastic tracking is applied, the basic interaction between droplets and continuous phase keeps the same, accounted by the source terms in the conservation equations. The source terms are not directly but rather indirectly affected by the stochastic method. For example, the drag force between droplets and the airflow depends on the slip velocity calculated by the averaged Navier-Stokes equations if without the stochastic tracking. With the stochastic tracking a random velocity fluctuation is imposed at an instant of time, and the drag force and additional convective heat transfer will be calculated based on this instantaneous slip velocity. The source terms associated with this instantaneous drag force and convective heat transfer enter the momentum and energy equations without any additional formulation. For a steady-state computation, the "instant of time" means "each iteration step." Therefore, the averaged momentum equation will not be affected by the stochastic tracking scheme; rather the trajectory of the droplet will reflect the effect of the imposed instantaneous perturbation.

### 2.5 Devolatilization Models

After all the moisture contained in the coal particle has evaporated, the particle undergoes devolatilization. Four different devolatilization models are employed and compared in this study, namely the Kobayashi model, single rate model, constant rate model, and CPD (Chemical Percolation Devolatilization) model. .

(a) Kobayashi model --- The Kobayashi model with two-competing devolatilization rates are expressed as a weighted function of two competing rates, $k_1$ and $k_2$, as shown below,

$$\frac{m_v(t)}{(1 - f_{w,0}) m_{p,0} - m_a} = \int_0^t (\alpha_1 k_1 + \alpha_2 k_2) \exp\left(-\int_0^t (k_1 + k_2) dt\right) dt \quad (31)$$

where $\alpha_1$ and $\alpha_2$ are yield factors, $f_w$ is mass fraction of moisture, $m_p$ is mass of particle, $m_a$ is mass of ash, and $R_1$ and $R_2$ are given as,

$$k_1 = A_1 e^{-(E_1/RT_p)} \quad (32)$$

and,

$$k_2 = A_2 e^{-(E_2/RT_p)}. \quad (33)$$

The value of the constants are $A_1 = 2x10^5$, $A_2 = 1.3x10^7$, $E_1 = 1.046x10^8$ J/kgmol, and $E_2 = 1.67x10^8$ J/kgmol.
The volatile matters contained in the coal are assumed to be composed of CO, $H_2$, and $C_6H_6$ [Tomeczek, 1994]. In this study, all of the volatile matters are lumped into one intermediate gas species whose release rate is given by Eq. (31). The intermediate gas species is assumed to be $CH_{1.952}O_{0.9278}N_{1.124}$ based on the coal property used in this study. Once this intermediate gas $CH_{1.952}O_{0.9278}$ is released, it is decomposed into the volatile gases – CO, $H_2$, and $C_6H_6$ – through Eq. (R1.7).

(b) Single rate model --- The devolatilization rate is dependent on the amount of volatiles remaining in the particle [Badzioch and Hawsley, 1970]. The devolatilization kinetic rate is defined in Arrhenius form below

$$k = Ae^{-(E/RT)} \quad (34)$$

where the pre-exponential factor, A, used in this study is $4.92x10^5$ and the activation energy, E, is $7.4x10^7$ J/kgmol.

(c) Constant rate model --- This model assumes that volatiles are released at a constant rate [Baum and Street, 1971]. The rate used in this study is **12/s** [Pillai, 1981].

(d) Chemical Percolation Devolatilization (CPD) model --- CPD model considers the chemical transformation of the coal structure during devolatilization. It models the coal structure transformation as a transformation of chemical bridge network which result in release of light gas, char, and tar [Fletcher and Kerstein (1992), Fletcher et. Al (1990), and Grant et. Al (1989)]. In this study, the volatile contained in the coal is assumed to be $C_6H_6$. The initial fraction of the bridges in the coal lattice is 1, and the initial fraction of char is 0. The lattice coordination number is 5. The cluster molecular weight is 400 and the side chain molecular weight is 50.

### 2.5 Combustion Models

Particle Combustion – The combustion of particle occurs after the devolatilization process has finished. The reaction rates for the solid-gas reactions are determined by kinetic reaction rates adopted from published literatures as presented in Table 1. The sources of these reaction rates are introduced and discussed below.

Field [1968] conducted an experiment to measure rate of reaction $C(s) + \frac{1}{2} O_2 \rightarrow CO$. Gas temperature used ranged from 1200K to 1720K at atmospheric pressure. Oxygen concentrations used ranged from 1% to 20%, and particle size ranged from 20μm to 100μm. The measured particle temperatures ranged from 1200K to 2000K.

It was assumed that the product formed inside the char and on the surface of the char was carbon monoxide and that on average CO was transported to some distance from the particle before it could combine with oxygen to form carbon dioxide. The reaction rate was calculated from the weight loss of a char sample in a given transit time at a given oxygen concentration. An overall reaction rate coefficient is defined as the rate of removal of carbon per surface unit external surface area per unit atmosphere partial pressure of oxygen in the gas. Field found that the variation of the diffusional reaction rate coefficient was not strong. The experiment did not detect any effect of particle size on the reaction rate. The kinetic reaction rate was found to be k = T(A+BT) where A = 0.067 m/(s-K) and $B = 5.26x10^{-5}$ m/s-$K^2$.

Mayers [1934(a)] conducted an experiment to determine the rate of reaction $C(s) + CO_2 \rightarrow 2CO$, where graphite was used as the C. The experiment was conducted at atmospheric pressure. Mayers measured the reduction rate of $CO_2$. The effects of diffusion as the rate determining factor were eliminated by increasing the gas velocity across the particle surface, thus removing the concentration gradients.

The rate of reduction of $CO_2$ through the reaction appeared in two temperature ranges: (a) 1120-1220K and (b) 1220-1570K. Mayers found that when $CO_2$ reacted with carbon at low temperatures (T < 1250K), CO was formed at the same rate as that at which $CO_2$ disappeared. This is explained by the retention of half of the oxygen of the carbon dioxide by the graphite ($C + CO_2 \rightarrow CO + C\text{-}O_{solid}$). Mayers indicated that the $CO_2$ reduction rate at the high temperature range might be represented by two reactions: $C + CO_2 \rightarrow CO + C\text{-}O_{solid}$ and $C\text{-}O_{solid} \rightarrow CO$, where the second reaction follows so rapidly on the first that there is no accumulation of $C\text{-}O_{solid}$. Thus the product of the $CO_2$ reduction is CO only. The $CO_2$ reduction rate is expressed in Arrhenius form $k = AT^n(-E/RT)$ where n = 1.0, A = -4.4 m/s-K, and $E = 1.62x10^{+8}$ J/kmol.

Mayers [1934(b)] conducted an experiment to measure the rate of $C(s) + H_2O(g) \rightarrow CO + H_2$, where graphite was used as the source of C, at atmospheric pressure in the temperature range of 1123-1433K under conditions which eliminated the effects of diffusion as the rate determining process. Mayers found that the appearance CO and of $CO_2$ varied rather widely within the same temperature group, but their sum was found to be constant. The ratio $CO/CO_2$ of the products of reaction depends on the speed of the secondary reaction ($CO + H_2O \rightarrow CO_2 + H_2$) and on the time during which the mixture of gases remains in the heated zone. The rate of oxidation of carbon by steam appeared in temperature ranges 1133-1233K and 1273-1433K. Mayers reported that the rate of oxidation of C was of the same order of magnitude as the rate of appearance of C as CO when graphite was oxidized by $CO_2$. The kinetic reaction rate was found to be $k = AT^n(-E/RT)$ where n = 1.0, A = -1.33 m/s-K, and $E = 1.47x10^{+8}$ J/kmol.

Gas Phase (homogeneous) Reactions – For the gas phase reactions, both the eddy-dissipation and finite rates are calculated, and the smaller of the two is used as the reaction rate. **Eddy-dissipation model** takes into account the turbulent mixing of the gases. It assumes that the chemical reaction is faster than the time scale of the turbulence eddies. Thus, the reaction rate is determined by the turbulence mixing of the species. The reaction is assumed to occur instantaneously when the reactants meet. The net rate of production or destruction of a species is given by the smaller of the two expressions below.

$$R = \nu' M A \rho \frac{\varepsilon}{k} \min\left(\frac{Y}{\nu' M}\right) \quad (35)$$

and

$$R = \nu' M B \rho \frac{\varepsilon}{k} \min\left(\frac{\Sigma Y}{\Sigma \nu' M}\right) \quad (36)$$

where $\nu'$ is the stoichiometric coefficient of reactant and $\nu''$ is stoichiometric coefficient of product. The smaller of the two expressions (35) and (36) is used because it is the limiting value that determines the reaction rate.

The **finite rate** does not take into account the turbulent mixing of the species. Reaction rate is expressed in an Arrhenius form. Reaction rates in Arrhenius form for all of the gas phase reactions are given in Table 2. For benzene oxidation, only the eddy dissipation is used.

Table 1. Reaction rates for solid-gas reactions

| *Reaction* | *Rate Constant* | *Parameters* |
|---|---|---|
| $C(s) + \frac{1}{2}O_2 \rightarrow CO$ (Combustion) | $k = T(A+BT)$ | A = -0.067 m/s.K<br>B = 5.26E-5 m/.s.K$^2$ |
| $C(s) + CO_2 \rightarrow 2CO$ (Gasification, Boudouard reaction) | $k = AT^n \exp(-E/RT)$ | n = 1.0<br>A = 4.4 m/s.K<br>E = 1.62E+8 J/kmol |
| $C(s) + H_2O(g) \rightarrow CO + H_2$ (Gasification) | $k = AT^n \exp(-E/RT)$ | n = 1.0<br>A = 1.33 m/s.K<br>E = 1.47E+8 J/kmol |

Table 2. Reaction rates for gas phase reactions

| Reaction | Rate Constant | Parameters |
|---|---|---|
| $CO + \frac{1}{2} O_2 \rightarrow CO_2$ | $k = AT^n \exp(-E/RT)$ | n = 0<br>A = 2.2x10$^{12}$<br>E = 1.67x10$^8$ J/kmol |
| $CO + H_2O(g) \rightarrow CO_2 + H_2$ (Watershift) | $k = AT^n \exp(-E/RT)$ | n = 0<br>A = 2.75x10$^{10}$<br>E = 8.38x10$^7$ J/kmol |
| $C_6H_6 + 3O_2 \rightarrow 6CO + 3H_2$ | Eddy-dissipation only | |

## 3.0 BOUNDARY AND INLET CONDITIONS

Indonesian coal is used as feedstock in this study. Its composition is given in Table 3 and the feed rates used are given in Table 4. The coal/water weight ratio of the coal slurry is 60%-40%. The oxidant used is 95% $O_2$ and 5% $N_2$. Oxidant/coal slurry feed rate used in Table 4 gives O/C (fixed carbon) value of 0.3. The temperatures of the slurry coal and the oxidant are 300K and 420K, respectively. Figure 2 presents the boundary conditions used in this study. The outlet is set as a constant pressure condition at 24 atm. The operating pressure inside the gasifier is at 24 atm.

The oxidant is considered as a continuous flow and coal slurry is considered as a discrete flow. The discrete phase only includes the fixed carbon and water which comes from the moisture content of the coal and from the water added to make the slurry. In other words, in the computational model, the slurry particle basically consists of a coal particle inside a water droplet. Other components of the coal, such as N, H, S, O, and ash, are injected as gas, together with the oxidant in the continuous flow. N is treated as $N_2$, H as $H_2$, and O as $O_2$. Reactions of S and ash are not simulated and they are lumped with $N_2$ as inert gases. The coal slurry size is uniformly given as 100, 200, 300 μm respectively for three different cases

Table 3. Composition of Indonesia Coal

| | Weight % |
|---|---|
| **Volatile** | 38.31% |
| **$H_2O$** | 8.25% |
| **ash** | 3.90% |
| **C** | 37.95% |
| **H** | 2.68% |
| **N** | 0.69% |
| **S** | 0.31% |
| **O** | 7.91% |
| **Total, wt %** | 100.00% |
| **HHV, kcal/kg** | 5690 |

Table 4. Feed rates used in the study

| | Feed rate (kg/s) |
|---|---|
| **Coal slurry** | 18.58 |
| **Oxidant** | 3.56 |

The walls are assigned as adiabatic with internal emissivity of 0.8. The boundary condition of the discrete phase at walls is assigned as "reflect", which means the discrete phase elastically rebound off once reaching the wall. At the outlet, the discrete phase simply escapes/exits the computational domain.

## 4.0 RESULTS AND DISCUSSIONS

### 4.1 Effects of Time Scale in the Stochastic Particle Tracking

Stochastic particle tracking employs the concept of integral time scale, which defines the time spent in turbulent motion along the particle path. The integral time scale can be calculated using the empirical formula $T = T_C\, k/\varepsilon$, where $T_C$ is the time constant, k is the turbulence kinetic energy and ε is the turbulence dissipation rate. The

suggested value of $T_C$ is 0.15. However, since this value of 0.15 was empirically obtained for a specific flow, it is not clear whether this value is adequate for the present thermal-flow field in a gasifier. Hence, a sensitivity study is conducted by comparing the results of using various $T_C$ values with the reference case without stochastic tracking (i.e. $T_C = 0$). The result in Fig. 4 shows that the mass-weighted temperature and various species distribution curves move closer to the reference curve when the $T_C$ value is decreased from 0.15 to 0.0015 but move away from the reference curve when the $T_C$ value is further decreased to 0.00015. By examining the hystereses effect of $T_C$'s influence, it seems the value 0.15 overcounts the random fluctuating effect of discrete particles. The result for $T_C = 0.00015$ is seen close to that of $T_C = 0.015$ and provides a comfortable upper and lower bounds of $T_C$ values which give consistent and similar results. Therefore, 0.015 is chosen instead of 0.00015 in this study as the value of $T_C$ to save calculation time because a larger $T_C$ value requires less integration during the stochastic tracking calculation.

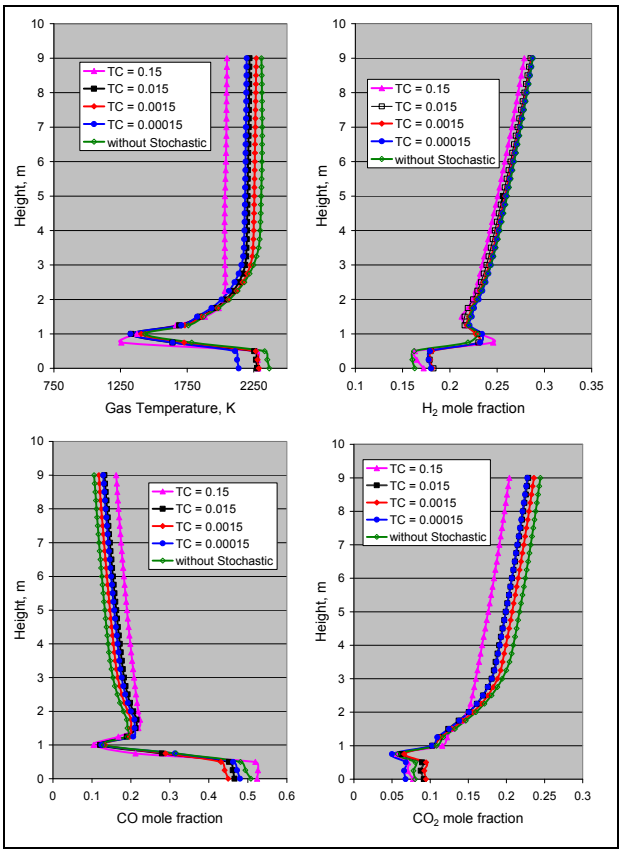


Fig. 4 Mass-weighted average temperature and species using standard k-ε model with different stochastic tracking $T_C$ (time scale) constants.

### 4.2 Effects of Turbulence Models

The effects of turbulence models are shown in Fig. 5 in terms of mass-weighted averages of temperature and species distribution along the height of the gasifier. The comparison shows that standard k-ε, RSM, and k-ω SST models give consistent and similar results while the results from the k-ω and k-ε RNG models deviate from the consistent trend. Further examination shows although standard k-ε, RSM, and k-ω SST give similar results above the fuel injection location, the results below the injection location show the k-ω SST model deviates from the standard k-ε and the RSM models. The similar results from the standard k-ε and the RSM models provide the advantage of using the standard k-ε model to conduct parametric studies to significantly save the computational time while the high-order RSM model is used to "verify" the relatively simpler standard k-ε model.

Regarding the k-ω SST model, although it is more complicated than the standard k-ε model by incorporating the low-Reynolds number effect and near-wall dissipation rate, it does not model the anisotropic Reynolds stresses as in the RSM model. Since the k-ω SST model does also confirm the consistency of the results of the standard k-ε model above the injection location, all the parametric studies are then conducted by the standard k-ε model to significantly save the computational time.

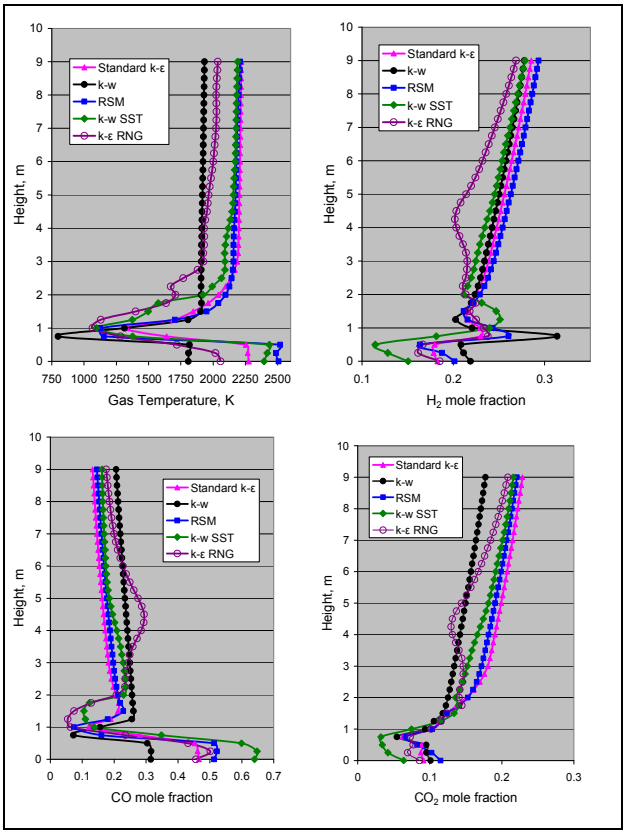


Fig. 5 Mass-weighted average temperature and species for cases with different turbulence models.

### 4.3 Effect of Devolatilization Models

Particle tracks for cases with different devolatilization rates are presented in Fig. 7. The overall tracks look very similar, except that the tracks for the Kobayashi model are a little bit longer. This means that the particle reaction (oxidation and gasification in Eq. R1.1. R1.2, and R1.3) finishes later than that of the other models. The VM

concentration contour plot in Fig. 7 also confirms that the devolatilization process using the Kobayashi model seems to starts later compared to other models with a smaller high-concentration core. Thus, it appears that the Kobayashi devolatilization model, which utilizes two weighted competing rates, is slower than the other models. Since particle reaction occurs after most of the moisture and volatiles have been released from the particle, as a result of the relatively slow devolatilization rate, the particle reaction starts and finishes much later compared to the other models.

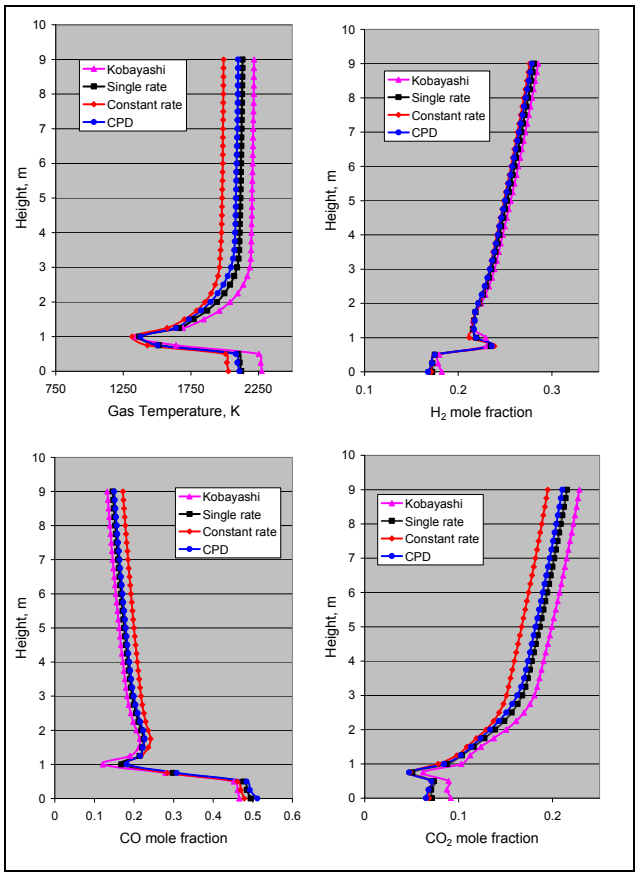


Fig. 6 Mass-weighted average temperature and species for standard k-ε model with different devolatilization models.

The particle tracks of the constant rate model and single rate model cases are very similar. The temperature and species distributions for both cases shown in Fig. 6 as well as the exit syngas composition listed in Table 5 are also similar. In summary, Kobayashi models predicts lower CO, but higher exit gas temperature, $H_2$, and $CO_2$, and hence lower gasification efficiency and lower heating value. CPD and single rate models produce more consistent results.

### 4.4 Effect of Particle Size

The coal slurry particles are assumed to be spherical. The coal slurry particle of 200 μm is assigned to the baseline case. Two other different coal slurry particle diameters, 100 μm and 300 μm, are also simulated for comparison. It is understood that the particle distribution in the real operation is not uniformly distributed. However, uniform particle size is assigned in each case to allow a more convenient way to track the change of particle size during the gasification process as well as to provide a clear comparison of the effect of particle sizes. The particle tracks presented in Fig. 7 show that 100-μm particles require more time to completely react than the 200-μm particles, which seems to be counterintuitive because the surface/volume ratio of smaller particle is larger than the larger particles and they should react more quickly. To look for explanation to this phenomenon, the focus is moved towards examining the relative motion between the particles and gases. Figure 8 presents side by side the particle tracks (discrete phase) and the streamlines of the continuous phase (gas). It can be seen that the tracks of the 100 μm particles follow the streamlines of the continuous flow; whereas the 200-μm particles deviate from the continuous flow streamlines. It seems that the deviation of the 200-μm particles from the streamlines increases the slip velocity which results in enhanced convective transports of heat and species concentrations. In the meantime, the mixing of the particles also augments particle reactions. Thus the 200-μm particles require less time to completely react than the 100-μm particles. When the particle diameter is increased to 300μm, the residence time for reaction increases. Other than the factor of reduced surface/volume ratio, it can be seen that the particles actually have much more inertia after fuel injection and are able to impinge on the opposite jet and split the particle streams in both above and below the injection location. Strong recirculation zones contribute to trapping particles and lengthen the residence time.

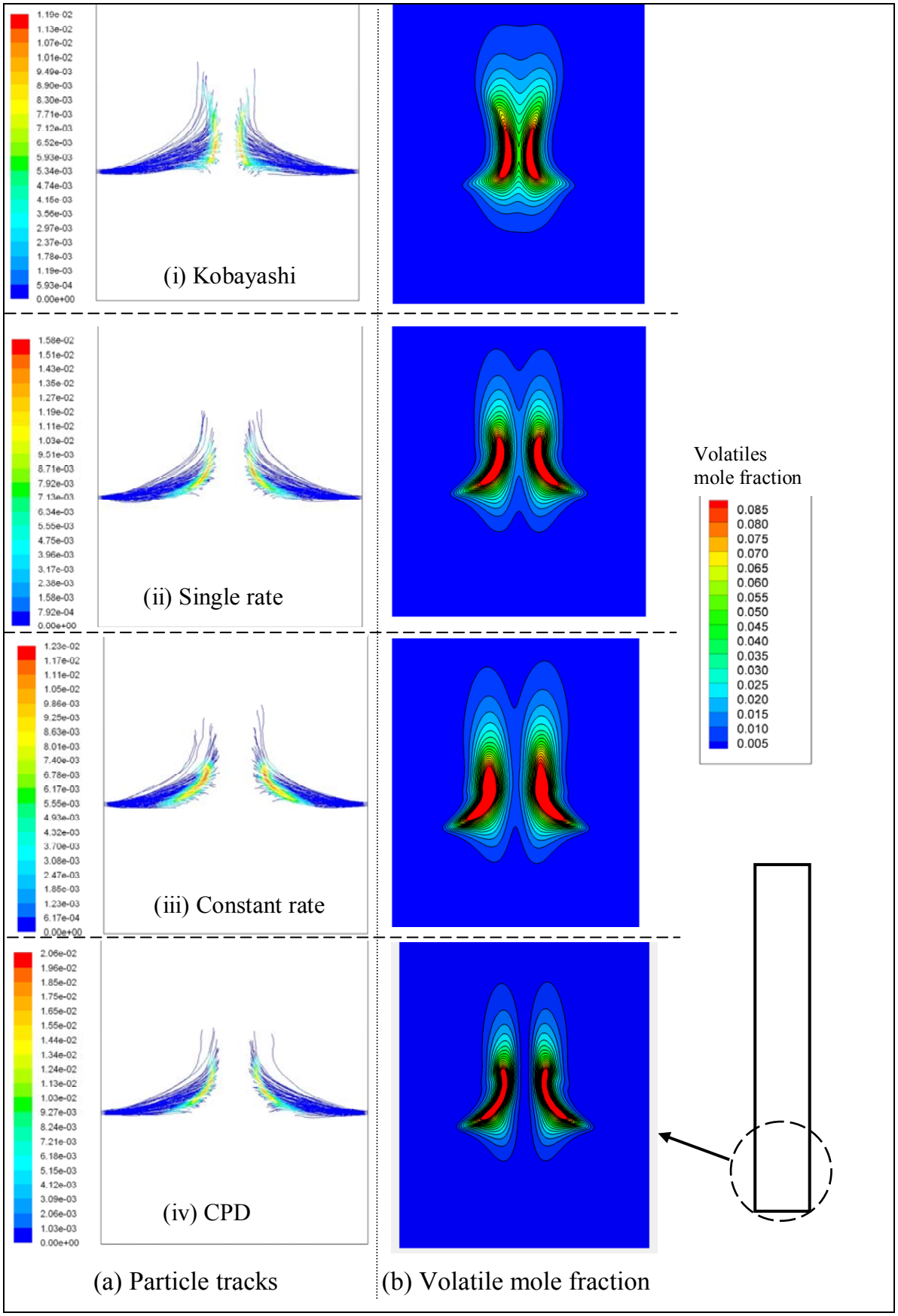


Fig. 7 Effect of four devolatilization models of 200-μm particle: (a) particle tracks colored by devolatilization rate (kg/s) and (b) volatiles mole fraction.

Table 5 Exit gas temperature and compositions for the 2D case with different devolatilization models.

| *Parameters* | *Kobayashi* | | *Single rate* | | *Constant rate* | | *CPD* | |
|---|---|---|---|---|---|---|---|---|
| Exit temperature, K | 2218 | | 2133 | | 1992 | | 2100 | |
| Components at exit: | | | | | | | | |
| | Mole fraction | Mole no. (mole) | Mole fraction | Mole no. (mole) | Mole fraction | Mole no. (mole) | Mole fraction | Mole no. (mole) |
| CO | 14.0% | 72.86 | 15.4% | 80.73 | 18.1% | 95.80 | 15.8% | 83.00 |
| $H_2$ | 28.9% | 150.41 | 28.5% | 149.41 | 28.1% | 148.72 | 28.2% | 148.14 |
| $CO_2$ | 22.9% | 119.19 | 21.5% | 112.71 | 19.5% | 103.21 | 21.0% | 110.31 |
| VM | 0.0% | 0.00 | 0.0% | 0.00 | 0.0% | 0.00 | 0.0% | 0.00 |
| $H_2O$ | 33.3% | 173.31 | 33.6% | 176.14 | 33.4% | 176.77 | 34.0% | 178.60 |
| $C_6H_6$ | 0.0% | 0.00 | 0.0% | 0.00 | 0.0% | 0.00 | 0.0% | 0.00 |
| $N_2$ | 0.9% | 4.68 | 1.0% | 5.24 | 0.9% | 4.76 | 1.0% | 5.25 |
| C | 0.0% | 0.00 | 0.0% | 0.00 | 0.0% | 0.00 | 0.0% | 0.00 |
| Heating value (MJ/kg) | 5.9 | | 6.1 | | 6.5 | | 6.1 | |

Mass-weighted temperature and species distribution curves in Fig. 9 show that there is a large exit temperature difference about 420K (1839 K vs. 2252K) between using smaller and larger particles (100 μm vs. 300 μm). The temperature near the gasifier bottom for the 300-μm case is much higher than those of the 100-μm and 200-μm cases. This is because the particles that impinge at the center and then go downward eventually burn out near the gasifier bottom. The exit syngas composition listed in Table 6 shows that the smallest particles give the highest syngas heating value. Generally speaking, larger particles produce more $H_2$, less CO, higher exit gas temperature, and more $CO_2$, and hence less efficient.

Table 6 Exit gas temperature and compositions for the 2-D case with different coal slurry sizes.

| *Parameters* | *100 μm* | | *200 μm* | | *300 μm* | |
|---|---|---|---|---|---|---|
| Exit temperature, K | 1839 | | 2218 | | 2252 | |
| Components at exit: | | | | | | |
| | Mole fraction | Mole no. (mole) | Mole fraction | Mole no. (mole) | Mole fraction | Mole no. (mole) |
| CO | 24.0% | 128.04 | 14.0% | 72.86 | 12.9% | 67.20 |
| $H_2$ | 26.3% | 140.31 | 28.9% | 150.41 | 29.8% | 155.25 |
| $CO_2$ | 15.5% | 84.13 | 22.9% | 119.19 | 23.8% | 123.99 |
| VM | 0.0% | 0.00 | 0.0% | 0.00 | 0.0% | 0.00 |
| $H_2O$ | 33.3% | 180.75 | 33.3% | 175.03 | 32.6% | 171.03 |
| $N_2$ | 0.9% | 4.89 | 0.9% | 4.73 | 0.9% | 4.72 |
| C | 0.0% | 0.00 | 0.0% | 0.00 | 0.0% | 0.00 |
| Heating value (MJ/kg) | 7.1 | | 5.9 | | 5.9 | |

### 4.5 Three Dimensional Gasifier

Using the parametric study of 2-D results, the selected turbulence model (standard k-ε turbulence), devolatilization model (Kobayashi) and stochastic tracking time constant ($T_C$ = 0.015) are employed to conduct 3-D gasifier simulation with 200 μm particles. The 3-D geometry in Fig. 2 is the same as the one used in the previous study by Wang and Silaen (2005), Bockelie et al. [2002(a)] and Chen et al. [2000]. The gasifier is a 2-stage gasifier, but only the first-stage injectors are used with the second-stage injectors being turned off. The first stage injectors consist of two levels of tangential injectors. Each level has four injectors. The diameter and the height of the gasifier is the same as that of the 2-D one.

The hottest region in the combustor section occurs in the region near the wall as pictured in Fig. 11. The $O_2$ distribution, also pictured in Fig. 11, shows that $O_2$ does not travel far from the injectors before it is fully depleted. Particle tracks from one injector given in Fig. 10 show that particle temperatures do not reach above 1000 K until the particles nearly reach the area of the next injector downstream at higher elevation. During that time, water evaporates and devolatilization follows. Once the particles have passed the downstream second-level injectors, they react with the $O_2$ injected through the second-level injectors. The top view shows that some high-temperature particles burn out near the wall and contributes to the high-temperature region near the combustor wall.

The exit gas temperature and syngas compositions are listed in Table 7. Exit gas temperature in the 3-D case is 1853 K, which is 400 K lower than that of the 2-D case. The 3-D case gives lower $H_2$ and $CO_2$ mole fractions (3.5 and 7.5 percentage points lower, respectively) and higher CO mole fraction (9.5 percentage points higher) than the 2-D case. The 3-D case results in 14% higher heating value (6.7 vs. 5.9 MJ/kg) as expected because 3-D domain provides longer residence time and allows better gasification performance.

Table 7 Exit gas temperature and compositions for the 3-D case compared to the 2-D case.

| *Parameters* | *2-D* | | *3-D* | |
|---|---|---|---|---|
| Exit temperature, K | 2218 | | 2133 | |
| Components at exit: | | | | |
| | Mole fraction | Mole no. (mole) | Mole fraction | Mole no. (mole) |
| CO | 14.0% | 72.86 | 23.5% | 293.06 |
| $H_2$ | 28.9% | 150.41 | 24.7% | 308.02 |
| $CO_2$ | 22.9% | 119.19 | 15.4% | 192.05 |
| VM | 0.0% | 0.00 | 0.0% | 0.00 |
| $H_2O$ | 33.3% | 173.31 | 35.6% | 443.95 |
| $N_2$ | 0.9% | 4.68 | 0.8% | 9.98 |
| C | 0.0% | 0.00 | 0.0% | 0.00 |
| Heating value (MJ/kg) | 5.9 | | 6.7 | |

## 5.0 CONCLUSIONS

Turbulence models significantly affect the simulated results. Among five turbulence models tested, the standard k-ε and the RSM models give consistent results.

The time scale for employing stochastic time tracking of particles affects simulated result. Caution has to be exerted to select the appropriate time constant value. In this study, the time constant value of 0.015 and 0.00015 produce consistent results.

Among four devolatilization models, the Kobayashi model produces slower devolatilization rate than the other models. The constant rate model produces the fastest devolatilization rate. The single rate model and the chemical percolation model produces moderate and consistent devolatilization rate. Slower devolatilization rate produces lower CO, but higher exit gas temperature, $H_2$, and $CO_2$, and hence both the heating value and gasification efficiency are lower.

Usually smaller particles have larger surface/volume ratio and react more quickly than larger particles. However, it is discovered that larger particles possess higher inertia after injection. Higher inertia produce higher slip velocity which increases higher convective transport and hence higher reaction rate. High inertia can also propel the particles cross the gas streamlines and increase particle-gas mixing which results in enhanced reaction rate. When the inertia continue increases as particle size increases, the injection jet impinges on the opposite jet and results in strong recirculation zones which can trap the particles and increase the residence time. Using the results of parametric study in 2-D cases, appropriate models are selected for 3-D simulation to gain more confidence of the 3-D results.

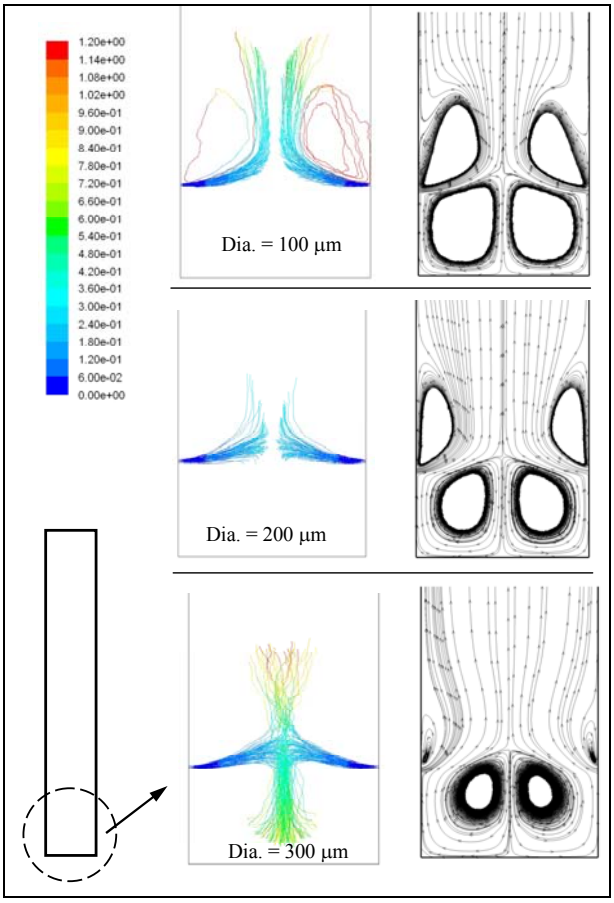


Fig. 8 Particle tracks and gas streamlines show effect of different coal slurry particle sizes. The particle tracks are colored by residence time (s). Kobayashi devolatilization model is used.

## 6.0 ACKNOWLEDGEMENTS

This study was supported by the Louisiana Governor's Energy Initiative via the Clean Power and Energy Research Consortium (CPERC) and administered by the Louisiana Board of Regents.

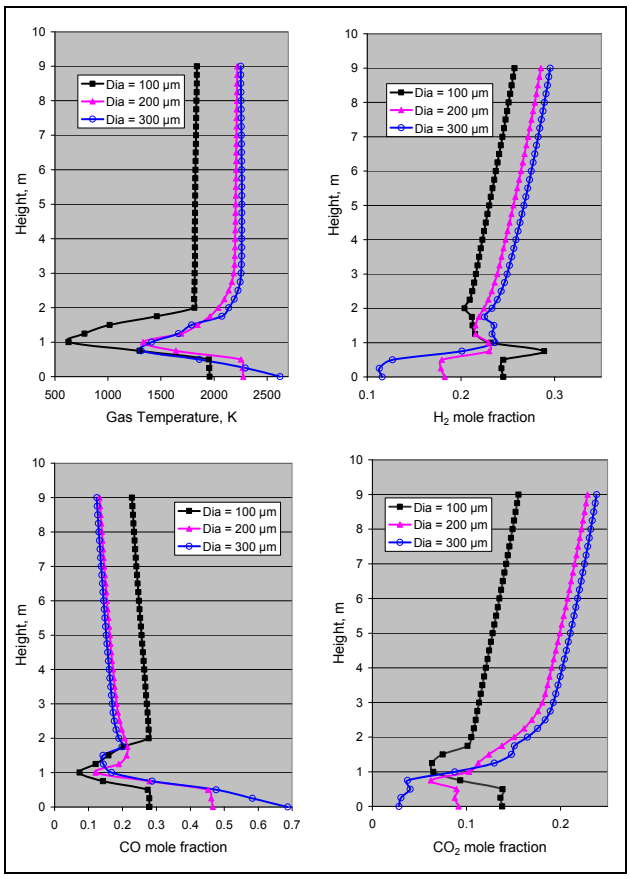


Fig. 9 Mass-weighted average temperature and species distributions for standard k-ε model with different coal slurry particle sizes.

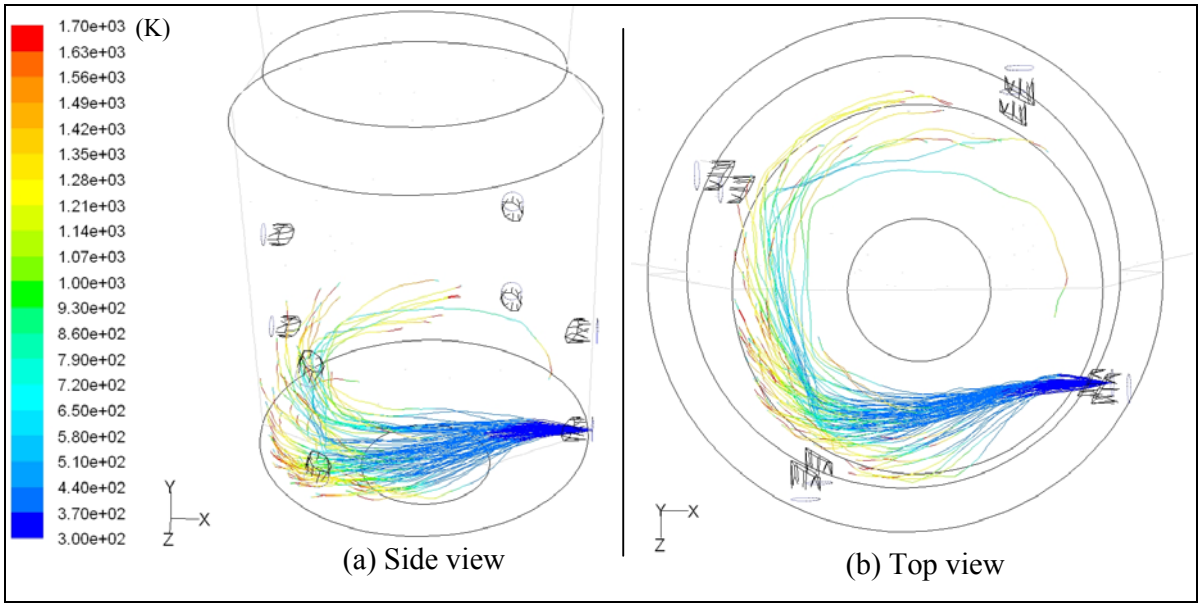


Fig. 10 Particle tracks colored by particle temperature in the combustor section of the 3D gasifier. For clarity, only one injection is shown.

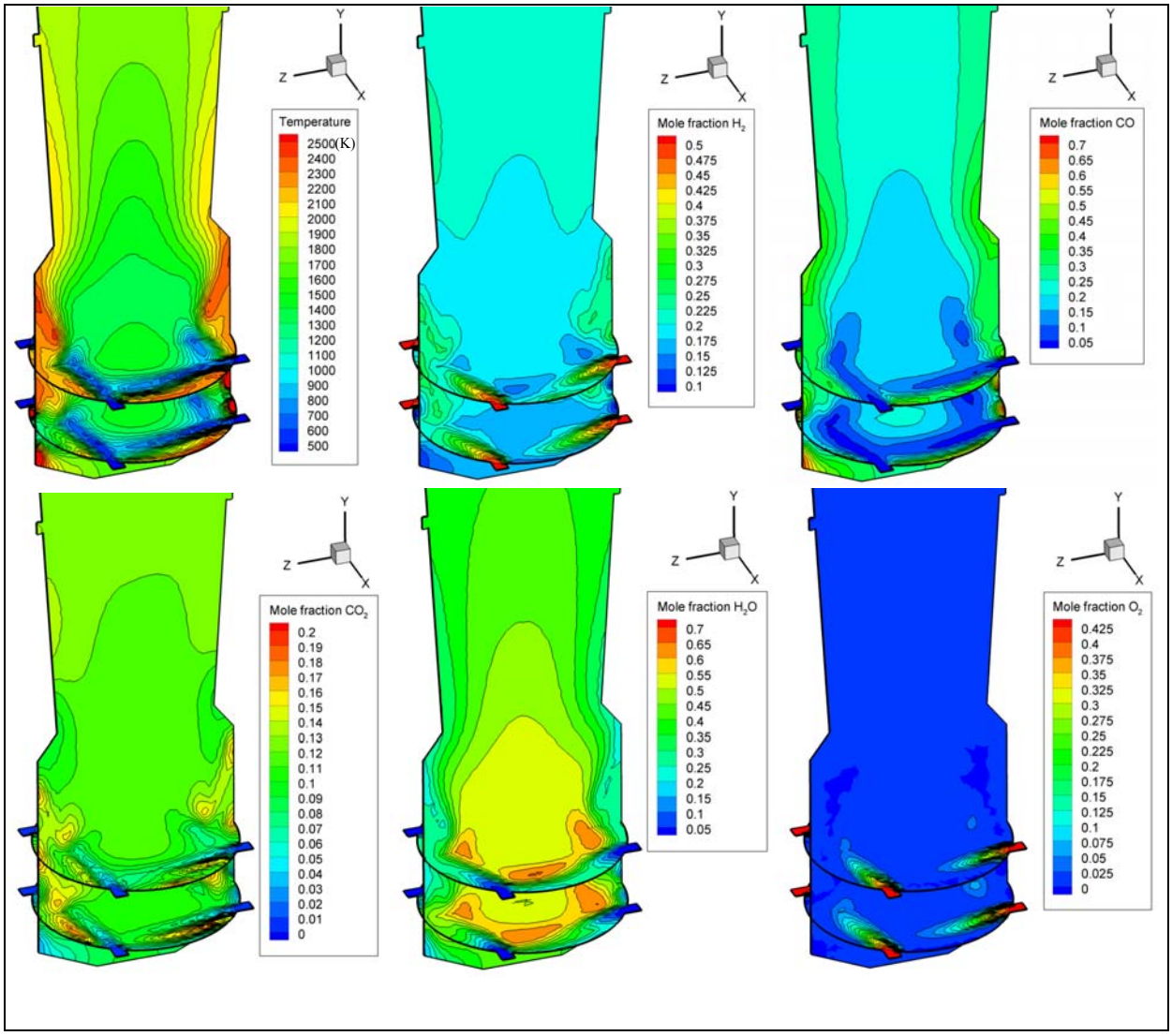


Fig. 11 Temperature and species distributions in the combustor section of a 3-D gasifier

## REFERENCES


Badzioch S., and Hawsley P.G.W., Kinetics of Thermal Decomposition of Pulverized Coal Particles, Ind. Eng. Chem. Process Design and Development, Vol. 6, pp. 521-530, 1970.

Baum, M.M., and Street, P.J., Predicting the Combustion Behavior of Coal Particles, Combustion Science Technology, Vol. 3, pp. 231-243, 1971.

Bockelie, M.J, Denison, K.K., Chen, Z., Linjewile, T., Senior, C.L., and Sarofim, A.F., CFD Modeling For Entrained Flow Gasifiers in Vision 21 Systems, Proceedings of the 19th Annual International Pittsburgh Coal Conference, Pittsburgh, PA. Sept 24-26, 2002(a).

Bockelie, M.J, Denison, K.K., Chen, Z., Linjewile, T., Senior, C.L., and Sarofim, A.F., CFD Modeling For Entrained Flow Gasifiers, Proceedings of the Gasification Technologies Conference 2002, San Francisco, CA, Oct. 28-30, 2002(b).

Chen, C., Horio, M., and Kojima, T., Numerical Simulation of Entrained Flow Coal Gasifiers, Chemical Engineering Science, **55**, 3861-3833, 2000.

Choudhury, D., 1993, Introduction to the Renormalization Group Method and Turbulence Modeling, Technical Memorandum, TM-107, Fluent Inc

Field, M.A., Rate of Combustion of Size-Graded Fractions of Char From a Low-Rank Between 1200 K and 2000 K, Combustion and Flame, Vol. 13, pp. 237-252, 1968.

Fletcher, T.H., and Kerstein, A.R., Pugmire, R.J., Grant, D.M., Chemical Percolation Model for Devolatilization: 2. Temperature and Heating Rate Effects on Product Yields, Energy and Fuels, 4, 54, 1990.

Fletcher, T.H., and Kerstein, A.R., Chemical Percolation Model for Devolatilization: 3. Direct Use of $^{13}C$ NMR Date to Predict Effects of Coal Type, Energy and Fuels, 6, 414, 1992.

FLUENT 6.3 User's Guide, September 2006.

Grant, D.M., Pugmire, R.J., Fletcher, T.H., and Kerstein, A.R., Chemical Percolation of Coal Devolatilization Using Percolation Lattice Statictics, Energy and Fuels, 3, 175, 1989.

Lauder, B.E., and Spalding, D.B., Lectures in Mathematical Modeling of Turbulence, Academic Press, London, England, 1972.

Lauder, B.E., and Spalding, D.B., The Numerical Computation of Turbulent Flows, Computer Methods in Applied Mechanics and Engineering, 3:269-289, 1974.

Magnussen, B.F., and Hjertager, On mathematical models of turbulent combustion with special emphasis on soot formation and combustion. In 16th Symp. (Int'l) on Combustion. The Combustion Institute, 1976.

Mayers, M.A., The Rate Reduction of Carbon Dioxide by Graphite, Journal of American Chemical Society, Vol. 56, pp. 70-76, 1934(a).

Mayers, M.A., The Rate Oxidation of Graphite by Steam, Journal of American Chemical Society, Vol. 56, pp. 1879-1881, 1934(b).

Menter, F, 1993, "Zonal Two Equation Model for Aerodynamic Flows," AIAA Paper 93-2906.

Patankar, S.V., Numerical Heat Transfer and Fluid Flow, McGraw Hill, 1980.

Pillai, K. K., The Influence of Coal Type on Devolatilization and Combustion in Fluidized Beds, Journal of Inst. Energy, 1981.

Singh, C. P. P., and Saraf, D. N., Simulation of High-Temperature Water-Gas Shift Reactors, Ind. Eng. Chem. Process Des. Dev., 16, pp. 313-319, 1977.

Silaen, A. and Wang,T., Simulation of Coal Gasification Process Inside a Two-Stage Gasifier, Paper-007, Proceedings of the 22nd Pittsburgh Coal Conference, Pittsburgh, Pennsylvania, September 19-22, 2005.

Silaen, A. and Wang,T., Effects of Fuel Injection Angles on Performance of A Two-Stage Coal Gasifier, Paper 20-4, Proceedings of the 23rd Pittsburgh Coal Conference, Pittsburgh, Pennsylvania, September 25-28, 2006.

Smoot, D.L., and Smith, P.J., Coal Combustion and Gasification, Plenum Press, 1985.

Tomeczek J., Coal Combustion, Krieger Publishing Company, 1994.

Wilcox, D.C., 1998, Turbulence Modeling for CFD, DCW Industries, Inc., La Canada, California.